Wind buffeting effects on the Gemini 8m primary mirrors

M. K. Cho[1,2], L. Stepp[1], and S. Kim[3]

Gemini Preprint #75

(1) Gemini Observatory, 950 N. Cherry Ave., Tucson AZ 85721
(2) Optical Sciences Center, University of Arizona, 1630 E. University Blvd, Tucson, Arizona 85721
(3) Aerospace and Mechanical Engineering, University of Arizona, 1130 N. Mountain, Tucson, AZ 85721

Wind buffeting effects on the Gemini 8m primary mirrors

Myung K. Cho[1,2], Larry Stepp[1], and Seongho Kim[3]

(1) Gemini 8m Telescopes Project; (2) Optical Sciences Center, University of Arizona; (3) Aerospace and Mechanical Engineering, University of Arizona

ABSTRACT

One of the critical design factors for large telescopes is control of primary mirror distortion caused by wind pressure variations. To quantify telescope wind loading effects, the Gemini Observatory has conducted a series of wind tests under actual mountaintop conditions. During commissioning of the southern Gemini Telescope, simultaneous measurements were made of pressures at multiple points on the mirror surface, as well as wind velocity and direction at several locations inside and outside the dome. During the test we varied the dome position relative to the wind, the telescope elevation angle, the position of windscreens in the observing slit, and the size of the openings in the ventilation gates. Five-minute data records were made for 116 different test conditions, with a data-sampling rate of ten per second. These data sets have been processed to provide pressure maps over the surface of the mirror at each time instant. From these pressure maps, the optical surface distortions of the primary mirror have been calculated using finite-element analysis. Data reduction programs have been developed to enhance visualization of the test data and mirror surface distortions. The test results have implications for the design of future large telescopes.

Keywords: wind buffeting, large telescopes, structure function, Gemini Observatory

1. INTRODUCTION

Large telescopes are particularly susceptible to wind loading - as telescopes get larger, the structural deflections caused by wind loading increase and the resonant frequencies of the telescope structure decrease, which brings them closer to the range of peak energy in the wind gust spectrum. This not only affects pointing and tracking – uneven wind loading can also distort the figure of the primary mirror. For telescopes of 8-m class or larger, one of the key performance factors is to control the distortion of the primary mirror caused by wind loading. Since some wind flow across the telescope is desirable to avoid problems with thermally induced local seeing, the need for ventilation must be balanced against the problems caused by wind buffeting.

A number of studies have been conducted to quantify wind-buffeting effects on large astronomical telescopes. Forbes[1] gives an extensive list of references on this subject. Many studies have investigated the effect of wind loading on primary mirror distortion. Some have been based primarily on theoretical calculations[2]. Other studies[3] have used sub-scale wind tunnel measurements; but with scale factors typically between 1:30 and 1:100 there are well-known limitations caused by lack of similarity in flows having very different Reynolds numbers. Several studies[4,5,6] have combined wind tunnel tests with numerical modeling of wind flow. This can provide a valuable cross reference to verify and calibrate the wind tunnel measurements, but due to computational limitations, the numerical models have incorporated only simple shapes to represent the telescope and dome.

Actual wind measurements at observatory sites are very valuable, of course, and several measurement programs have been conducted at existing observatories[7,8,9]. However, these have all had limitations. The studies reported in references 7 and 8 placed pressure sensors above the mirror covers of existing 4-meter class telescopes, but both studies used very limited numbers of pressure sensors (four and five, respectively). Extrapolations from such a limited set of locations are prone to large errors.

The ESO study described by Noethe, et al[9] used a 3.5-meter plywood dummy mirror instrumented with 13 pressure sensors. It was placed in the enclosure of the NTT (in front of the telescope) and also in an inflatable dome prototype, both at La Silla in Chile. The angle of the plywood panel was varied in elevation, and tests were run with the dummy mirror at different azimuth orientations relative to the wind. Much useful data was obtained from this testing program, and the Gemini Project based part of its initial analysis of wind buffeting on ESO's data. Huang[10] calculated the response of the Gemini primary mirror to various static and dynamic pressure patterns based on the La Silla data. However, the pressure measurements at each sensor were independently recorded, so dynamic pressure patterns had to be inferred from the temporal RMS variations at each sensor.

During the integration of the second Gemini 8-meter Telescope in 2000, there was an opportunity to conduct a series of wind tests while the dummy primary mirror was in the telescope. The Gemini Observatory provided an excellent test bed for making wind pressure measurements, since:

1. The tests could be conducted at full scale in an 8-meter telescope
2. The Gemini dummy mirror has similar dynamic properties to the real primary mirror
3. The test mirror could be in the actual position of the primary mirror in the telescope
4. The Gemini enclosures have large adjustable ventilation gates[11], so measurements could be made in a range of conditions from a fully-protected telescope embedded in its enclosures, to a telescope almost fully open to the wind.

Ultrasonic anemometers were installed at several locations on the telescope and above the dome, and the surface of the dummy primary mirror was instrumented with pressure sensors (24 for the first series of tests, then 32 for the second series).

During the first series of tests, several dozen sensitive accelerometers were placed at various points on the telescope structure by our collaborators from the Modal Analysis & Controls Laboratory of the University of Massachusetts Lowell. Simultaneous measurements of wind velocity and pressure on the primary mirror were recorded at 10 Hz in conjunction with telescope dynamic tests. The dynamic information was recorded at faster rates by a separate data acquisition system, but synchronization of the data was established by recording the wind velocity readings on both data acquisition systems. The first series of tests has previously been described in several papers and reports[12,13,14].

The principle goals of the wind test were:
1. Improve our understanding of wind effects on the Gemini primary mirrors
2. Evaluate the validity of the mathematical and numerical models that were developed earlier in the design stage
3. Learn how to best set the adjustable vent gates depending on wind speed and direction
4. Extrapolate the wind measurements on an 8-meter telescope to apply to larger telescopes.

The extrapolation is aided by the fact that the Gemini primary mirrors are located above the elevation axis, where they are quite open to the wind flow (as compared to other designs where the primary mirror is down in a well created by the telescope center section). This configuration has similarities to many of the conceptual designs for future extremely large telescopes.

2. WIND TEST SETUP

2.1 Test setup and coordinate system

The Gemini dummy primary mirror is a ribbed steel structure with a continuous convex back surface and an open ribbed top. It has approximately the same mass and center of mass location as the real primary mirror, and was designed to have the same fundamental resonant frequency. Its attachment to the mirror supports is the same as the real primary mirror. For this test, the dummy mirror was covered with plywood to represent the mirror surface.

The coordinate system used in the wind test is based on a right-handed Cartesian system. The local coordinate X-axis is parallel to the telescope elevation axis, positive from left to right looking at the primary mirror optical surface with the telescope pointing at the horizon. The Z-axis defines the optical axis, positive from the primary mirror to the secondary mirror. The origin of this coordinate system is defined to be at the vertex of the optical surface of the primary mirror.

In the initial wind tests in conjunction with the dynamic structural measurements, a total of 114 different sensors were monitored. The test setup consisted of 74 channels of acceleration, 1 channel of force, 24 channels of pressure, and 15 channels of wind speed (three orthogonal measurements from each of five anemometers). Of these, 103 were monitored simultaneously in the wind tests: 62 accelerometers, together with the 24 pressure sensors and 15 channels of wind speed data.

In the second series of wind tests, eight more pressure sensors were added around the outer edge of the dummy primary. Also, a sixth anemometer (three more channels) was added at the +Y axis, but it failed early in the second test series. The accelerometers were removed before the second series of tests.

2.2 Data acquisition hardware and software

A National Instruments I/O board ("777516-01 National Instruments PCI-6033E I/O Board") was installed in a Pentium PC system. This board was used to record the wind pressure data and wind speeds from the anemometers. A connector block box (SCB-100, shielded, 100 pins) was used in conjunction with a shielded interface cable assembly. LabView software was used to collect the data. The integrated system is shown in Figure 1.

2.3 Wind pressure sensors

The pressure sensors were Setra model 264 bi-directional differential pressure transducers with a range of ± 50 N/m^2. Differential pressure measurements were monitored at the sensor ports (high and low) connected by plastic tubes. The high port is connected to a copper orifice flush with the plywood surface of the dummy mirror.

The pressure taps are in a square grid over the 8-meter dummy primary, as shown in Figure 2.

Figure 1. Interface cables and connector block for the wind sensors.

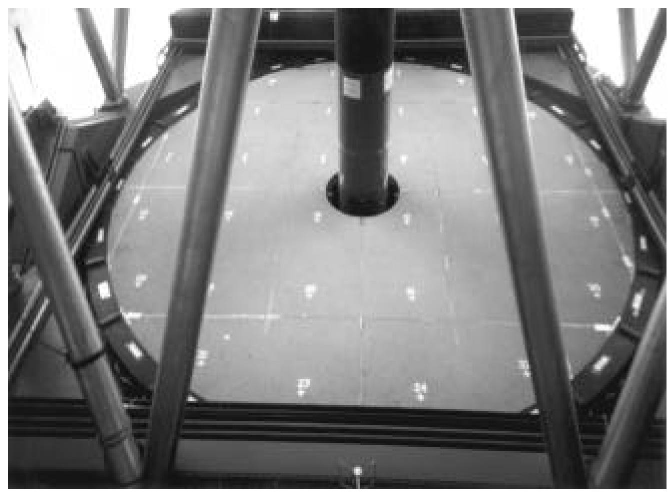

Figure 2. Wind pressure sensors on dummy primary mirror.

2.4 Wind velocity sensors (anemometers)

The anemometer used in the wind test was a model 8100 ultrasonic anemometer from R.M. Young Company. The anemometer can measure three orthogonal wind velocities ultrasonically. These wind velocities were calibrated and recorded at 10 Hz for an interval of five minutes for each of the wind tests.

The six anemometer locations were:

- two locations above the telescope elevation axis (+X and –X axes)
- at the top and bottom side (horizon pointing) of the primary mirror cell (+Y and –Y axes)
- behind the secondary mirror assembly (M2 location)
- at the top of the dome (Dome location)

3. TEST PROCEDURES

Simultaneous measurements were made of pressures at multiple points on the mirror surface, as well as the wind velocity and direction at several locations inside and outside of the dome. The data collections for the wind pressure and the wind velocity are “in phase” — there is no time delay among the sensor readings. During the test we varied: (1) the dome position relative to the wind; (2) the telescope elevation angle; (3) the position of windscreens in the observing slit; and (4) the size of openings of the ventilation gates.

The file name of the test case encodes the test setup and the conditions of the test. The first character identifies the test set depending on the test dates, test study cases, or test setups (24 or 32 pressure sensors). The following three numbers in the name indicate the azimuth orientation of the dome slit relative to the incoming wind direction. The next two numbers indicate the zenith angle of the telescope, and the final two letters indicate the status of the large vents on the side of the Gemini enclosure, the first letter indicating the upwind vent gate and the second letter the downwind vent gate. So, for example, 04530oc indicates the telescope was pointing 45 degrees away from the wind in azimuth, at a zenith angle of 30 degrees (elevation of 60 degrees), the upwind vent gate was open and the downwind vent gate was closed.

Two types of dynamic structural tests were performed for the first series of tests: impact modal testing with a measured force input; operating data testing using the wind as the structural excitation. There were 44 wind/operating tests performed on the structure under varying conditions, of which 40 also have pressure and wind speed data.

A second series of 76 tests filled in more combinations of test conditions (azimuth angle, zenith angle, windscreen position, vent gate openings).

4. TEST DATA REDUCTION

4.1 Wind pressure readings

Five-minute data records were made for each of the 116 tests, with pressure and wind speed data sampled at ten times per second. Each test record therefore has data for 3000 time intervals.

The readings from the wind pressure transducers were recorded as voltages. To convert voltage to pressure in Pascal (Pa) or (N/m^2), the following conversion formula was used:

$$\text{Pressure (Pa)} = (\text{Pressure reading (Volts)} - V_0) * 20 \text{ (Pa/Volt)} \tag{1}$$

where V_0 is the 5-minute average voltage output of each sensor under approximately zero wind loading conditions (vent gates and shutter closed).

The total range of the pressure sensors is 0-5 V, corresponding to $\pm$ 50 Pa; thus, the zero offset is generally about 2.5 V. The sensitivity is a nominal value from the manufacturer's data sheets. Variation in the sensitivity of any single sensor over its 0-5 V operating range is given by the manufacturer as <1%.

These data sets have been processed to provide pressure maps over the surface of the mirror at each time instant. From these pressure maps, the optical surface distortions of the primary mirror have been calculated using finite-element analysis. An animation graphics program has been developed to enhance visualization of the test data and the mirror surface distortions.

Before the pressure data is used for wind spectra calculations, we need to measure the response spectrum of the sensors and adjust the data accordingly. However, Smith[15] removed the DC bias for Power Spectral Density (PSD) information and assumed that any variation in the actual sensitivity acts only to shift the entire PSD vertically.

4.2 Wind velocity readings

As described for the pressure sensors, the data record for each wind velocity sensor consists of 3000 sample readings "in phase". These readings from the transducers were recorded as voltages. To convert voltage to pressure in units of meters per second (m/s), we used the following formula:

for sensors inside the dome:

$$\text{Velocity (m/s)} = (\text{Velocity reading (Volts)} - V_0) * 5 \text{ (m/s/V)} \tag{2}$$

for the dome sensor:

$$\text{Velocity (m/s)} = (\text{Velocity reading (Volts)} - V_0) * 10\ (\text{m/s/V}) \quad (3)$$

The total range of the wind sensors is 0-4 V, and the nominal zero value V_0 is calibrated to be 2.0 V as found in the manufacturer's data sheet. The anemometer electronics were set to a velocity range of ±10m/s for the inside sensors, and ± 20 m/s for the dome sensor.

As with the pressure transducers, the sensitivity we used is the nominal value from the manufacturer's data sheet. We have no separate calibration information on the sensors, however, as with the pressure sensors, for PSD information we remove the DC bias and any variation in the actual sensitivity will act only to shift the entire PSD vertically[15].

The wind speed measured on top of the dome is different from the free stream wind speed, and since the anemometer was not centered on top of the dome, the difference depends on the direction of the wind. Calibration runs were made comparing the wind velocity measured on top of the dome to the velocity at the weather tower about 100 meters away. From this data correction factors have been calculated, ranging from 0.47 to 2.18.

4.3 Average and RMS calculations

The measured wind pressures and velocities vary with location of the sensors (spatial distribution) and with time (temporal distribution). The overall average of the wind pressure was calculated as follows:

$$\text{Average global pressure: } P_{gavg} = < P_j >, \text{ for } j = 1 \ldots N_s \quad (4)$$

where N_s is the number of pressure sensors, and P_j is the temporal average of the pressure at the jth sensor:

$$Pj = < Pj(ti) > \quad (5)$$

where ti is the time of the ith sample, i = 1…3000

The calculated average represents the spatial average first, followed by the temporal average. The same P_{gavg} is independent of the order, since the raw average is linear.

The average spatial RMS of the wind pressure was calculated as follows:

$$\text{Average spatial RMS pressure: } Prms = < (Prms)_i >, \text{ for } i = 1 \ldots 3000 \quad (6)$$

where $(Prms)_i$ is the spatial RMS pressure at the ith time instant.

For wind velocity calculations at each of the anemometer locations, the following formulas were used:

$$\text{Velocity at the 'ith' time step: } V_i = \text{sqrt}\,(Vx_i^2 + Vy_i^2 + Vz_i^2) \quad (7)$$
$$\text{Temporal average velocity magnitude: } V_{avg} = < V_i > \quad (8)$$
$$\text{Velocity RMS: } V_{rms} = \text{sqrt}\,(< (V_i - V_{avg})^2 >) \quad (9)$$

where Vx, Vy, and Vz are wind velocities in X, Y, and Z direction, respectively.

5. TEST RESULTS

5.1 Wind velocity

For each 5-minute data set, the following information has been calculated from the wind velocity data:

- instantaneous resultant wind speed at each anemometer
- average resultant wind speed at each anemometer
- average resultant wind speed in three anemometers around the primary mirror (M1)
- corrected outside wind speed based on dome anemometer reading
- ratio of average wind speed at M1 compared to outside wind speed
- ratio of average wind speed at M2 compared to outside wind speed

The results can be categorized in terms of the test conditions, for example, according to the positions of the adjustable vent gates. Table 1 gives the average ratio of wind speed at M1 compared to outside wind speed, and the average ratio of wind speed at M2 compared to outside wind speed, for four different vent combinations.

Vent Gate Positions (upwind-downwind)	Relative wind speed at M1	Relative wind speed at M2
Closed-Closed	13%	64%
Closed-Open	37%	74%
Open-Closed	35%	57%
Open-Open	74%	61%

Table 1. Effect of vent gate positions on average attenuation of outside wind velocity.

As expected, the wind speed at the primary mirror is attenuated significantly more when the vent gates are closed. Interestingly, the wind speed at M2 is relatively unchanged by the vent gates, in fact, there may be a slight decrease in relative wind speed at M2 when the vent gates are opened.

5.2 Wind pressures

For each 5-minute data set, the following information has been calculated from the pressure data:

- maximum and minimum pressure at each sensor
- average pressure at each sensor
- time history of the average pressure over the mirror
- average pressure on the mirror surface
- average total force normal to the mirror (F_z)
- average moment about the X-axis
- average moment about the Y-axis
- temporal average of the spatial RMS pressure

For selected tests, frequency response functions have been calculated using a fast Fourier transform in Matlab. Figure 3.a shows the time history of the pressure reading at a single sensor in one of the tests. Figure 3.b shows the frequency response function of the pressure variation at that sensor, calculated from the time history.

Figure 4.a shows the time history of the (spatial) average pressure over the mirror in the same test. Notice that lower gust frequencies become more visible in the averaged data, with periods as long as 50-100 seconds. Figure 4.b shows the frequency response function for the average pressure.

For each measurement interval in each test, the pressure readings at the 24 or 32 sensors have been interpolated and extrapolated over the mirror surface by means of a cubic spline fit to produce a surface pressure map. Examples are shown in the second column of Figures 5 and 6.

From these pressure maps the resulting mirror surface deformations have also been calculated using the Finite Element Method. Since the lowest resonance frequency of mirror bending modes is above 15 Hz, the deformations from the measured data are quasi-static and are therefore directly proportional to the loading. Examples of the mirror deformation maps are shown in the third column of Figures 5 and 6. The mirror deformations have been analyzed in a number of ways, including calculation of peak-to-valley and RMS amplitudes after subtraction of piston, tip-tilt and focus, derivation of Zernike polynomial coefficients and calculation of the approximate Strehl ratio. The RMS mirror deformations have been averaged for each test to provide a measure of the effect of the wind loading on image quality.

Pressure maps have also been created for the average pattern of pressure for each test. Examples are shown in the first column in Figures 5 and 6.

The wind loading on the primary mirror is strongly dependent on the amount the vent gates are open, as can be seen by comparing Figures 5 and 6, which are plotted to the same color scale. In both figures the telescope and enclosure are oriented into the wind and the telescope is pointing 30 degrees from the zenith. The two measurements were taken only a few minutes apart and the average outside wind speed was equivalent within a few percent.

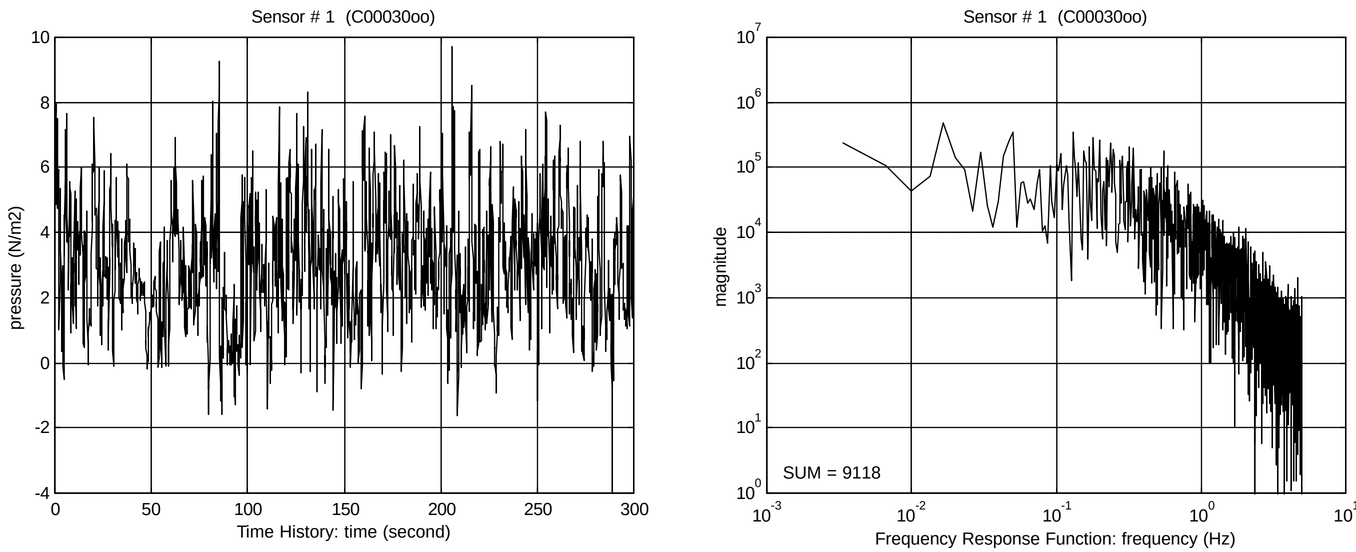

Figure 3. (a) (b) Time history and frequency response function of wind pressure sensor #1.

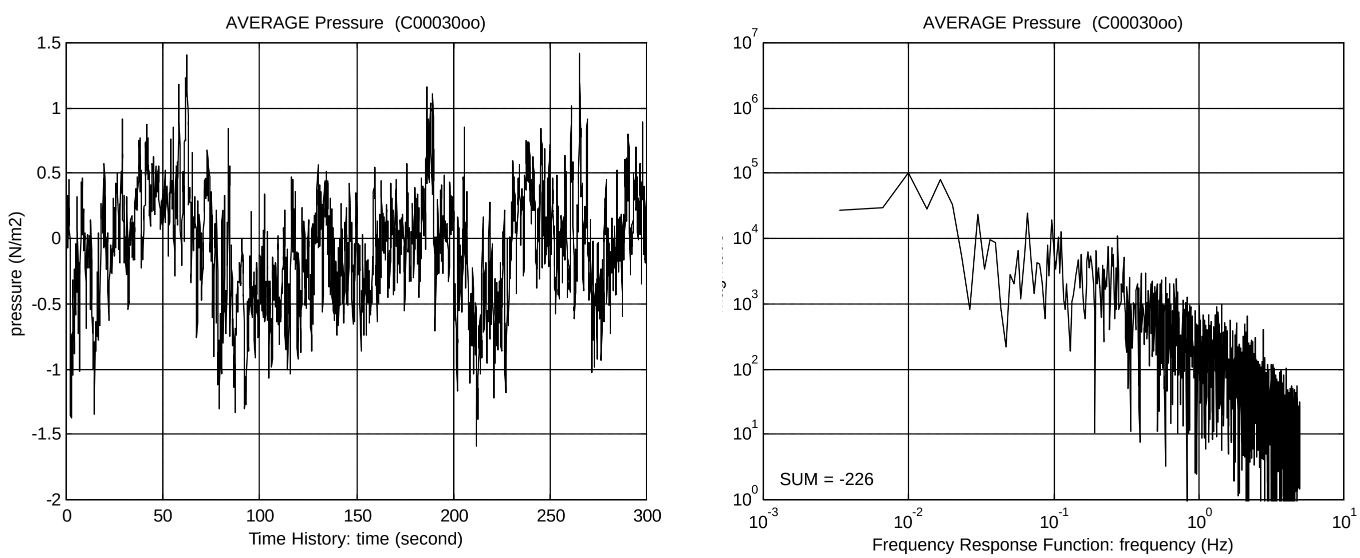

Figure 4. (a) (b) Time history and frequency response function of spatial average wind pressure.

In Figure 5 both vent gates are closed. Figure 5.a represents the average pressure pattern on the mirror; the full color scale represents ± 10 N/m^2. Figure 5.b is a pressure map from a particular time (19.2 seconds into the test) plotted to the same scale. Figure 5.c is the resulting mirror surface deformation; the full color scale represents ± 1 micron. The average total normal force and moments for this test were:

Fz = -7 N
Mx = 8 N-m
My = -16 N-m

In Figure 6 both vent gates are open. Both the pressure variations and mirror deformations are an order of magnitude higher than in the closed-closed case. The average total normal force and moments for this test were:

Fz = 26 N
Mx = 151 N-m
My = -10 N-m

Note that the instantaneous pressure pattern in each case has a significantly higher amplitude than the quasi-static pressure pattern represented by the average pressures.

5.3 Animations of test results

The color plots of wind pressure patterns and mirror deformations have been combined into animation files that run at the same 10 Hz rate as the data collection. This makes it possible to watch the pressure patterns flickering over the mirror surface at real-time rate, and see a representation of the mirror deformations that result. To facilitate understanding of the wind conditions, the resultant wind speed at each of the anemometers is shown on a gage that is part of the animation.

The scale of the plots has been maintained the same in all 116 animation sequences. Regions in red represent positive values, regions in blue represent negative values. The full range on the pressure plots is ± 10 N/m^2. The full range on the deformation plots is ± 1 micron. The wind speed gages have a range of 0-20 m/sec.

Short versions of the animations of all the test cases can be found at the following Web address:

http://www.aura-nio.noao.edu/studies/wind_tests3/index.html.

These animations contain the first 100 frames of the data (10 seconds at 10 samples per second). Figure 7 is an example frame from the animation of test case c000300oo.

5.4 Structure functions

One of the goals of the wind study is to understand how the information obtained at the 8-meter scale can be extrapolated to even larger future telescopes. One issue is whether the wind gusts are well correlated over significant distances. Smith, et al[13] compared the pressures at pairs of sensor locations and found some coherence between adjacent sensors, but a weaker coherence between sensors farther apart.

To investigate this subject further, structure functions have been calculated from the measured pressures on the surface of the dummy primary mirror. The pressure structure function, D(ρ), is a measure of how the amplitude of pressure differences from one point to another on the mirror surface varies as a function of the separation between the measurement points. It is defined for homogeneous and isotropic wind pressure as[17]:

$$D(\rho) = \langle \, | P(r+\rho) - P(r) |^2 \, \rangle \qquad (10)$$

where D(ρ) is a mean square of the pressure difference between two points on the mirror surfaces; P is wind pressure; ρ is a sensor spacing; and r represents a position on the mirror surface.

The structural function for wind test case c00030oo is shown in Figure 8. For each test, a structure function plot was calculated for each of the 3000 time intervals, and these values were averaged for each of the possible separation distances in the grid of sensor locations to produce the final plot.

Structure functions have been calculated for each of the 116 tests. A power law curve has been fitted to each structure function. The amplitudes of these fitted curves vary by a factor of 90 depending on the test conditions. The exponents of the curves vary from 0.35 to 0.63 with an average of 0.49 and standard deviation of 0.08.

Structure functions of all the test cases can be found at the following Web address:

http://www.aura-nio.noao.edu/studies/wind_tests2/index.html.

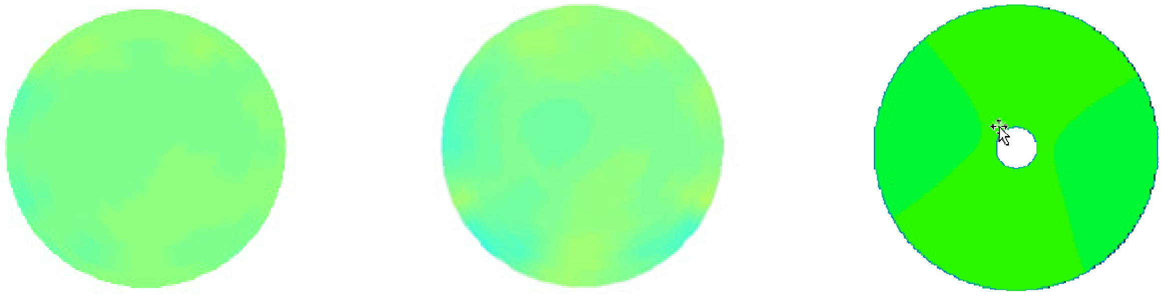

(a) Average pressure pattern
RMS = 0.17 N/m^2

(b) Pressure pattern at t = 19.2 seconds
RMS = 0.35 N/m^2

(c) Mirror surface deformation
RMS = 0.03 micron

Figure 5. Pressure and surface deformation plots for test case c00030cc (azimuth angle 0, zenith angle 30 degrees, both vent gates closed).

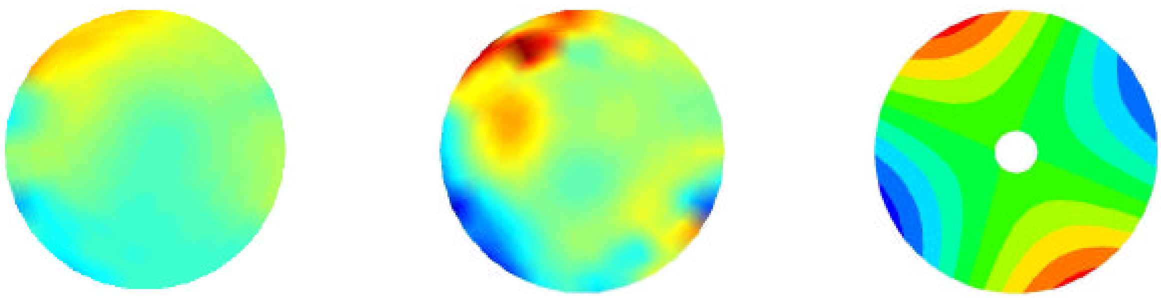

(a) Average pressure pattern
RMS = 1.48 N/m^2

(b) Pressure pattern at t = 19.2 seconds
RMS = 2.67 N/m^2

(c) Mirror surface deformation
RMS = 0.03 micron

Figure 6. Pressure and surface deformation plots for test case c00030oo (azimuth angle 0, zenith angle 30 degrees, both vent gates open).

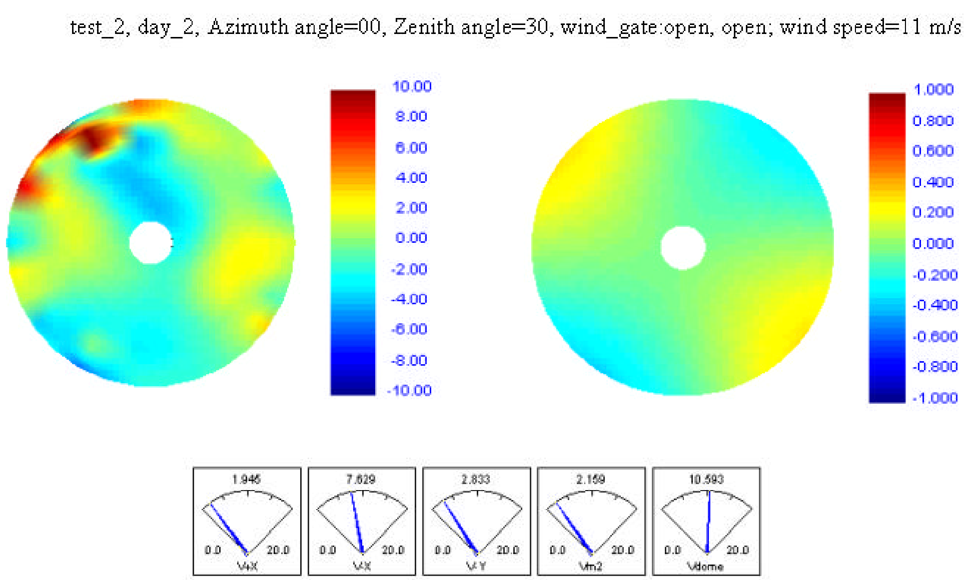

Figure 7. A single frame from the animation of wind pressure, wind speed, and mirror deformation for test c00030oo.

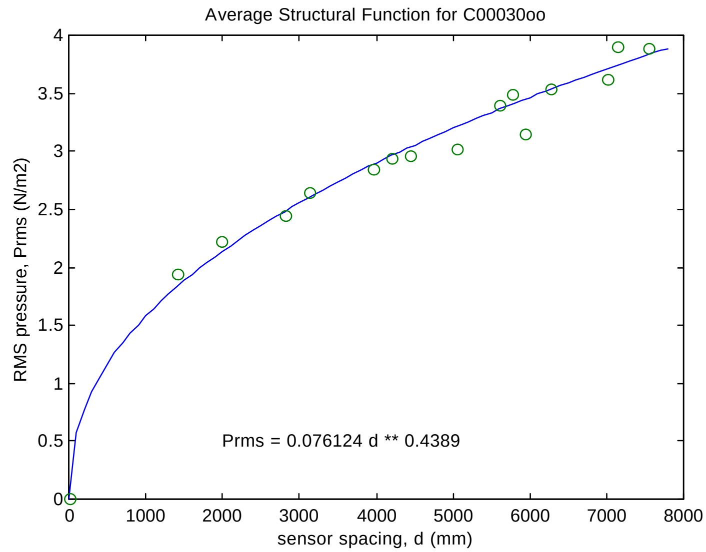

Figure 8. Average Structure Function for wind test case c00030oo.

5.5 Mirror deformation as a function of pressure variation and wind speed

Another goal of the test has been to understand how the mirror deformations depend on wind parameters, so we can develop rules to control the Gemini vent gate positions to provide good flushing with ambient air while maintaining the figure of the primary mirror within the error budget. Figure 9 shows the RMS mirror deformations plotted as a function of the RMS pressure variations. Each point in Figure 9 represents the average values for one of the tests. Not surprisingly, the mirror deformations are linearly proportional to the magnitude of the RMS pressure variation. The points clustered tightly in the lower left corner are the cases in which both vent gates are closed.

Figure 10 is a plot of RMS mirror deformation as a function of average wind speed at the primary mirror. A best-fit parabola is also shown, and it can be seen that the deformations vary approximately as the square of the wind speed at the mirror. The error budget for wind-induced deformation of the primary mirror is 60 nm RMS. On the best-fit curve, this corresponds to a wind speed of about 3 m/sec.

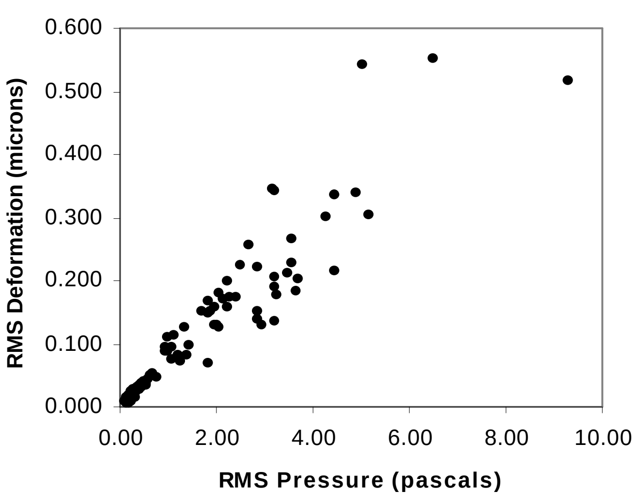

Figure 9. RMS mirror deformation as a function of RMS pressure variation.

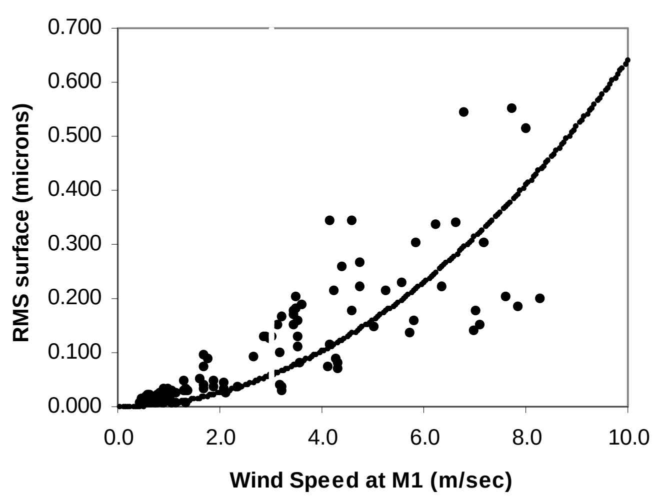

Figure 10. RMS mirror deformation as a function of average wind speed at the primary mirror.

There is some variation in the effect of the wind at different azimuth orientations. For a given wind speed at the primary mirror, the wind has a greater effect on the mirror when the telescope is facing into the wind and less effect when the telescope is facing away. Fitting the best fit values for eight azimuthal positions to a cosine curve, the rule for allowable wind speed at the primary mirror is:

$$V_{M1} < 3.2 - (0.8 \text{ x } \cos \theta) \quad (11)$$

where θ is the angle between the incoming wind direction and the direction the direction the telescope is pointing.

The Gemini vent gates will be adjusted to allow wind through the enclosure, up to the allowable wind speed at the primary.

5.6 Comparison to previous modeling assumptions

Zago[2] discussed telescopes in open air (with little or no enclosure) and indicated the wind load could be described by a static term corresponding to a uniform drag pressure, plus a dynamic term smaller in magnitude by a factor of two or more. This clearly does not describe the situation inside the Gemini enclosure, where the dynamic portion of the pressure pattern is usually larger than the static portion, and the static portion is not uniform. In fact, the average RMS pressure pattern is one to two orders of magnitude higher in amplitude than the average pressure on the mirror, which is close to zero for most tests. The pressures on the mirror are negative almost as often as they are positive.

Huang[10] calculated the predicted deformations of the Gemini primary mirror from pressure maps derived from ESO data. His results show deformations 2-8 times as large as would be produced using the average ratio of deformation to pressure RMS amplitude from the current study. It appears this may be partly because the pressure input in the earlier study was in terms of low-order Zernike polynomials, while the measured-interpolated wind patterns in this study tend to be higher spatial frequency and therefore do not couple as effectively to the low-order mirror bending modes.

DeYoung[16] describes numerical analysis of wind flow in the Gemini enclosures. Qualitatively, several of his findings correlate with our results. For the telescope facing into the wind, he found similar velocity attenuation factors at the secondary mirror. He predicted that, with the vent gates open, attenuation of the wind velocity at the location of the primary would be greater when the telescope pointed into the wind than when the telescope pointed at 90 degrees to the wind, which we verified experimentally. However, the attenuation ratios do not match particularly well. This could be not only because of the simplified geometry of the numerical model, but there may be a difference in what we are calling the free wind stream velocity. We hope to conduct additional tests to investigate this further. In one area there was a clear difference. DeYoung’s Figure 18 shows a predicted pressure pattern over the primary mirror for the telescope facing into the wind and inclined to a zenith angle of 30 degrees. The average pressure pattern we measured for this orientation is similar in shape (essentially a linear gradient) but opposite in sign. This could be because the numerical model of the mirror was a simple cylinder, while the real mirror is surrounded by telescope structure that influences the airflow.

Early modeling of the effect of wind loading on the telescope structure assumed a power spectral density (PSD) of the form shown by the straight line sections in Figure 11. PSDs calculated from the measured wind data, scaled to the same amplitude, have a very similar form as shown by the dashed line.

6. CONCLUSIONS

1. As expected, the wind velocity and pressure at the primary mirror are strongly influenced by the position of the vent gates.

2. The vent gate positions have little effect on the wind velocity at the secondary mirror.

3. With vent gates open, the attenuation of wind velocity at the primary mirror is higher when facing into the wind than when at 90 degrees to the wind.

4. Time-varying pressure patterns on the primary mirror are larger than the average pressure pattern.

5. The optical surface deformations of the Gemini primary mirror due to wind pressures are dominated by astigmatic modes.

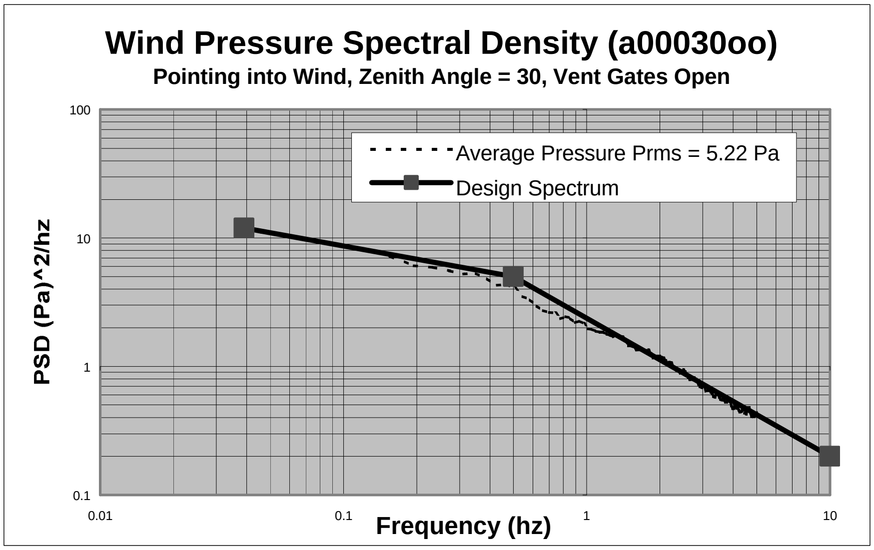

Figure 11. Comparison of measured power spectral density to spectrum assumed in Gemini design studies (figure courtesy of Mike Sheehan).

6. The RMS mirror deformation is linearly proportional to the RMS pressure variation.

7. The RMS mirror deformation is approximately proportional to the square of the wind velocity.

8. The Gemini error budget for wind-induced deformation of the primary mirror will typically be met if the wind velocity at the primary mirror follows the rule described in equation 11.

9. Structure functions of the wind pressures on the primary mirror tend to follow a ½ power law. If this is extrapolated to a 30-meter telescope, the range of wind pressure on the primary mirror would be expected to be about twice the amplitude on an 8-meter mirror, for a similar enclosure.

ACKNOWLEDGEMENTS

The authors would like to acknowledge the support of the Gemini staff on Cerro Pachon in setting up and performing the wind tests, particularly John Roberts, Gabriel Perez, Pedro Gigoux, Manuel Lazo, Pablo Prado and Mike Sheehan, who also helped with data interpretation. We would like to thank David Smith of MERLAB for organizing the dynamic measurements and collaborating in the data reduction. Special thanks are also extended to Earl Pearson and Teresa Bippert-Plymate for their helpful review and comments.

The Gemini Observatory is operated by the Association of Universities for Research in Astronomy, Inc., under a cooperative agreement with the NSF on behalf of the Gemini partnership: the National Science Foundation (United States), the Particle Physics and Astronomy Research Council (United Kingdom), the National Research Council (Canada), CONICYT (Chile), the Australian Research Council (Australia), CNPq (Brazil) and CONICET (Argentina).

REFERENCES

1. F. F. Forbes, "The Effects of Wind Loads on Large Telescopes and Their Enclosures", *Very Large Telescopes and Their Instrumentation*, ed. M.-H. Ulrich, ESO Conference and Workshop Proc. No. 30, pp. 831-843, Garching, Germany, 1988.
2. Lorenzo Zago, "Environmental effects and enclosure design for large telescopes", *Very Large Telescopes and their Instrumentation*, ed. M.-H. Ulrich, ESO Conference and Workshop Proc. No. 30, pp. 815-830, Garching, Germany, 1988.
3. R. E. Belcher, G. R. Stacey and C. J. Wood, "Wind effects on a proposed 8 m optical telescope", University of Oxford Department of Engineering Science report O.U.E.L. 1736/88, 1988.
4. J.-A. Hertig, C. Alexandrou and Lorenzo Zago, "Wind tunnel tests for the ESO VLT", , *Very Large Telescopes and Their Instrumentation*, ed. M.-H. Ulrich, ESO Conference and Workshop Proc. No. 30, pp. 855-866, Garching, Germany, 1988.

5. Michael Schneermann, “VLT Enclosures wind tunnel tests and fluid dynamic analyses,” *Advanced Technology Optical Telescopes V*, ed. L. Stepp, Proc. 2199, pp. 465-476, SPIE, Kona, Hawai’i, 1994.
6. Zhengqiu Yao, Xiangqun Cui, Denbin Tan, Zhilin Zhang, “LAMOST enclosure and its wind load analysis”, *Telescope Structures, Enclosures, Controls, Assembly/Integration/Validation, and Commissioning*, ed. T. Sebring and T. Andersen, Proc. 4004, pp. 164-172, SPIE, Munich, Germany, 2000.
7. Fred Forbes, George Gabor, “Wind loading of large astronomical telescopes”, *Advanced Technology Optical Telescopes*, ed. L. Barr, Proc. 332, pp. 198-205, SPIE, Tucson, Arizona, 1982.
8. N. Itoh, I. Mikami, T. Noguchi, Y. Shimizu, Y. Yamashita, J. Sovka, R. McLaren, A. Erasmus, “Mechanical structure of JNLT -- Analysis of mirror deflection due to wind loading”, *Advanced Technology Optical Telescopes IV*, ed. L. Barr, Proc. 1236, pp. 866-877, SPIE, Tucson, Arizona, 1990.
9. L. Noethe, M. Mornhinweg, M. Ravensbergen, M. Sarazin, G. Timmermann and L. Zago, “Pressure measurements with a dummy mirror and the implications for the design of the enclosure and the support of the primary mirror of the VLT”, ESO VLT Project technical report, 1992.
10. Eugene Huang, “Response of the Primary Mirror to Wind Loads”, Gemini Project technical report RPT-O-G0035, 1993.
11. Keith Raybould, Robert Ford, Paul Gillett, Steve Hardash and Gordon Pentland, “Gemini Enclosure and Support Facility Design Philosophy and Design Description,” *Advanced Technology Optical Telescopes V*, ed. L. Stepp, Proc. 2199, pp. 452-464, SPIE, Kona, Hawai’i, 1994.
12. Peter Avitable, Johann Teutsch, Keith Weech, David Smith, Geoff Gwaltney and Michael Sheehan, “Modal and operating characterization of an optical telescope”, *Proceedings of the 19th International Modal Analysis Conference*, Kissimmee, FL, 2001.
13. Smith, D.R., Weech, K., Teutsch, J.T., Avitabile, P., Gwaltney, G., Sheehan, M., and Cho, M., Comparison of Pressure Measurements and Operating Data for Wind Excitation of Telescope Structures," *Proceedings of the 19th International Modal Analysis Conference*, Kissimmee, FL, 2001.
14. David Smith and Peter Avitabile, “Gemini South 8m Optical Telescope, Final Report,” MACL Report # 05-08570-001 2000.
15. David Smith, “Gemini South Wind Data”, Release 2.0, 2001.
16. David S. De Young, “Numerical Simulations of Airflow in Telescope Enclosures”, The Astronomical Journal, Vol. 112, No. 6, pp. 2896-2933, 1996.
17. Robert Tyson, *Principals of Adaptive Optics*, Academic Press, INC., 1991.